Space Weather

RESEARCH ARTICLE
10.1029/2019SW002382

Identifying Critical Input Parameters for Improving Drag-Based CME Arrival Time Predictions

C. Kay[1,2], M. L. Mays[1], and C. Verbeke[3]

[1]Heliophysics Science Division, NASA Goddard Space Flight Center, Greenbelt, MD, USA, [2]Department of Physics, The Catholic University of America, Washington, DC, USA, [3]Centre of Mathematical Plasma-Astrophysics, Department of Mathematics, Catholic University of Leuven, Leuven, Belgium

Key Points:
- We study the sensitivity of drag-based arrival time models to input parameters
- Different precision on the input parameters are needed for different "strength" CMEs
- The arrival time tends to be more sensitive to CME parameters than solar wind parameters

Correspondence to:
C. Kay,
christina.d.kay@nasa.gov

Citation:
Kay, C., Mays, M. L., & Verbeke, C. (2020). Identifying critical input parameters for improving drag-based CME arrival time predictions. *Space Weather*, *18*, e2019SW002382. https://doi.org/10.1029/2019SW002382

Received 16 OCT 2019
Accepted 13 DEC 2019
Accepted article online 18 DEC 2019

Abstract Coronal mass ejections (CMEs) typically cause the strongest geomagnetic storms, so a major focus of space weather research has been predicting the arrival time of CMEs. Most arrival time models fall into two categories: (1) drag-based models that integrate the drag force between a simplified CME structure and the background solar wind and (2) full magnetohydrodynamic models. Drag-based models typically are much more computationally efficient than magnetohydrodynamic models, allowing for ensemble modeling. While arrival time predictions have improved since the earliest attempts, both types of models currently have difficulty achieving mean absolute errors below 10 hr. Here we use a drag-based model ANTEATR (Another Type of Ensemble Arrival Time Results) to explore the sensitivity of arrival times to various input parameters. We consider CMEs of different strengths from average to extreme size, speed, and mass (kinetic energies between 9×10^{29} and 6×10^{32} erg). For each scale CME, we vary the input parameters to reflect the current observational uncertainty in each and determine how accurately each must be known to achieve predictions that are accurate within 5 hr. We find that different scale CMEs are the most sensitive to different parameters. The transit time of average strength CMEs depends most strongly on the CME speed, whereas an extreme strength CME is the most sensitive to the angular width. A precise CME direction is critical for impacts near the flanks but not near the CME nose. We also show that the Drag-Based Model has similar sensitivities, suggesting that these results are representative for all drag-based models.

Plain Language Summary Large explosions of plasma and magnetic field known as coronal mass ejections (CMEs) frequently erupt from the solar atmosphere. When CMEs head toward Earth, they interact with the near-Earth plasma and magnetic field, affecting the "space weather." CMEs typically cause the strongest space weather effects, so a major focus has been predicting the time it takes for a CME to propagate from the Sun to the Earth. Many models have been developed over the past decades to predict the arrival time of CMEs, but all have difficulty achieving absolute errors less than 10 hr. Here we use a simple model that integrates the drag force between a CME and the background solar wind. Due to the model's simplicity, we can run a large number of simulations, allowing us to explore how the arrival time changes as the various model inputs are changed. We consider CMEs of different strengths and find that the behavior differs between average and extreme CMEs. We determine the precision needed for each input parameter to achieve predictions that are accurate within 5 hr. We compare our results with those from a similar model. Both models exhibit the same sensitivity to the input parameters, suggesting that these results are representative for most drag-based models.

1. Introduction

Space weather refers to the state of the near-Earth radiation and plasma environment, which often changes as a result of solar-driven activity. Understanding the behavior of this environment is crucial as it can affect human technologies, both in space and on the Earth's surface, and adversely affect the health of humans in space. The latter is of particular relevance given NASA's renewed focus on human space exploration with a plan to return to the Moon by 2024 and eventually send humans to Mars.

Coronal mass ejections (CMEs) are large explosions of plasma and structured magnetic field that routinely erupt from the solar surface and continue propagating out through the solar system. CMEs drive some of the strongest space weather effects at Earth, so accurately predicting their arrival is essential.

Much focus has been placed on modeling the arrival time of CMEs, and most models follow the same basic algorithm. First, a CME is observed remotely near the Sun, and its basic properties, such as speed, size, and direction of propagation, are reconstructed using some sort of morphological model (e.g., Thernisien et al., 2006; Xie et al., 2004). These parameters are then used in a transit model that describes the interaction between the CME and the background solar wind through which it propagates. The duration determined from the transit model is combined with the time of the near-Sun observations to yield an arrival time at Earth.

Most arrival time models fall within three categories: empirical models, drag-based models, and magnetohydrodynamic (MHD) models. Empirical models use a relation between observable parameters and the transit time that is derived from a set of previously observed CMEs and their transit times. This is the simplest type of arrival time model with essentially instantaneous computation time. Notable examples include the Effective Acceleration Model (Paouris & Mavromichalaki, 2017) and the Empirical Shock Arrival or Empirical CME Arrival (Gopalswamy et al., 2001). In a similar manner, machine learning techniques can be used to generate simple arrival time models (Liu et al., 2018).

Drag-based models use a physics-based equation to calculate the drag between a CME and the background solar wind, which determines the CME velocity as a function of time as well as the arrival time. While more complicated than empirical models, drag-based models still tend to be fairly computationally efficient. These models tend to integrate similar forms of a standard drag equation, but the models vary greatly in dimensionality and the approaches used to represent the CME structure in a simplified manner. Examples include the Drag-Based Model (DBM; Vršnak et al., 2013), the Enhanced DBM (Hess & Zhang, 2015), the Ellipse Evolution Model (ElEvo; Möstl et al., 2015), a version of ElEvo using data from Heliospheric Imagers (ElEvoHi; Rollett et al., 2016), and a probabilistic version of the DBM (P-DBM; Napoletano et al., 2018).

The last type of model is full MHD models. These models simulate a full background solar wind and then simply embed a CME as either a hydrodynamic or magnetic structure at the inner boundary. The motion is then fully determined by the MHD equations, and the CME is not treated distinctly from the background solar wind. These models are the most sophisticated but also the most computationally expensive, making it currently impractical to use them for ensemble predictions before an actual CME arrival. These models differ in the approaches used for the background solar wind and how the CME is represented and embedded into the simulation. MHD models currently capable of arrival time predictions include SWMF AWSOM (Jin et al., 2017), ENLIL (Odstrcil et al., 2004), EUHFORIA (Pomoell & Poedts, 2018), and SUSANOO (Shiota & Kataoka, 2016).

While this process of predicting arrival times appears relatively straightforward, there are some subtleties. First, one should consider whether or not a CME will actually impact the Earth or it will miss it entirely. This is often not directly addressed in arrival time studies but is a critical aspect of space weather predictions. Second, if a CME travels faster than the speed at which information can propagate through the background solar wind, it will drive a shock wave ahead of it. Some arrival time models simulate the arrival of the shock, when present, while others focus on the main body of the CME. Both versions can be useful, but caution must be exercised when comparing with observations or between different models. Finally, most arrival time models require some level of human input, which can lead to different users obtaining different results. This difference from user to user is often only in determining the input parameters. Many morphological models are based on a visual best fit to observations rather than a deterministic value. In some cases, however, expert operators use the raw output from a deterministic model in combination with additional observations, and their experience to determine an arrival time (Riley et al., 2018), sometimes referred to as "forecaster-in-the-loop" or "human-in-the-loop."

To better understand the intricacies of predicting CME arrival time, the CME Arrival Time and Impact Working Team was formed (information at https://ccmc.gsfc.nasa.gov/assessment/topics/helio-cme-arrival.php) (Verbeke et al., 2019). This work was originally facilitated by NASA's Community Coordinated Modeling Center (CCMC) and is now a part of the International Space Weather Action Teams. As part of this project, the CCMC maintains the Arrival Time Scoreboard, a web-based system where modelers can submit their predictions for observed events before their actual arrival. As of 2019, the Arrival Time Scoreboard had over 20 registered models, roughly split between predicting the arrival time of the shock or the CME.

Verbeke et al. (2019) report on the current progress of the CME Arrival Time and Impact Working Team. The initial focus of the team has been to establish the parameters of a validation study. They have defined the metadata that should be collected, which will ensure that future model results are reproducible, as well as the metrics that will be used to assess the performance of each model. Finally, they have identified the CMEs that should be simulated and plan to produce a set of input parameters for each CMEs' size, speed, and location. Ensuring that all models are producing results for the same cases with the same inputs will greatly facilitate future comparison studies and better understanding of the difference between the models themselves.

Recently, Riley et al. (2018) analyzed the predictions submitted to the CCMC Arrival Time scoreboard. This combines results from 32 different models for 139 unique CMEs. Most models have predictions for fewer than 10 CMEs, making it difficult to assess their individual capabilities, but five models have predictions for more than 50 CMEs. For all cases, Riley et al. (2018) find an average error of −3.7 hr, indicating a slight bias toward early predictions. The mean absolute error is 12.9 hr, and the standard deviation is 17.1 hr, which are better measures for the accuracy of the model as positive and negative errors balance out in an unweighted average. We note that of these 32 models, eight of them use some form of the ENLIL model. Despite using the same core model, these eight can have very different results, showing the sensitivity to the chosen values of arrival time input parameters. Similarly, Wold et al. (2018) consider 279 CMEs impacting either Earth or one of the STEREO satellites and find an average absolute arrival time prediction error of 10.4 hr and an unsigned error of −4.0 hr using an ENLIL model.

Ensemble modeling can be a useful tool for more thoroughly characterizing arrival time predictions. One performs a set of model runs, or ensemble, each with slight variation in the input parameters, representing the typical range in their uncertainty from observations. Unlike a single instance of a model, the ensemble results give information on the range of possible arrival times, as well as the likelihood of each outcome. Pizzo et al. (2015) lay out much of the theoretical work for using arrival time ensembles for predictions using a version of ENLIL with a highly simplified solar wind background. A coarse-grid run requires about 30 s of computational time on a supercomputer, so an ensemble of 100 ENLIL simulations would require roughly an hour. While not impossible for individual studies, this computational requirement may not be sustainable for long-term operations, so alternative ensemble models may be preferable, such as the Drag-Based Ensemble Model (DBEM; Dumbović et al., 2018) which performs a ensemble of DBM models. For 25 CMEs, Dumbović et al. (2018) created ensembles of nearly 11,000 runs for each CME and found a mean absolute error of 14.3 hr. This error is comparable to the values found in the previous studies, and the simplicity of DBM allows for roughly 1,000 runs per second on a normal computer. Amerstorfer et al. (2018) performed an ensemble of ElEvoHI simulations for the 3 November 2010 CME, which impacted STEREO-B, and study the sensitivity of the transit time to specific input parameters.

In this work we use ensembles to address a specific question—which parameters need to be known the most accurately to improve arrival time predictions. Using a drag-based model, we perform large parameter space explorations and determine how the arrival time changes as each input parameter is varied. This information is essential as it will help focus future research strategies for improving arrival time predictions beyond the current mean absolute error of about 10 hr.

2. Model and Ensemble Parameters

We use ANother Type of Ensemble Arrival Time Results (ANTEATR; Kay & Gopalswamy, 2018) to study the sensitivity of drag-based arrival time modeling to various input parameters. ANTEATR was developed to take the output from ForeCAT (Kay et al., 2015), a model for the coronal deflections and rotations of CMEs due to background magnetic forces. Figure 1 shows the toroidal CME shape used in both ForeCAT and ANTEATR. The top of Figure 1 shows side and front views of the gray torus along with the location of the CME nose and flanks. The torus is assumed to have a circular cross section, but the toroidal axis (maroon dashed line) need not be circular. The toroidal direction points along the toroidal axis, and the poloidal direction points in/out of the page in the side view. In the front view, the poloidal and toroidal directions are shown with a dark blue and maroon arrows, respectively.

The CME shape is defined by the two semiaxis of the toroidal axis (light blue dashed lines marked a and c) and the cross-sectional width (light blue dashed line marked b). In practice, we define the torus using the

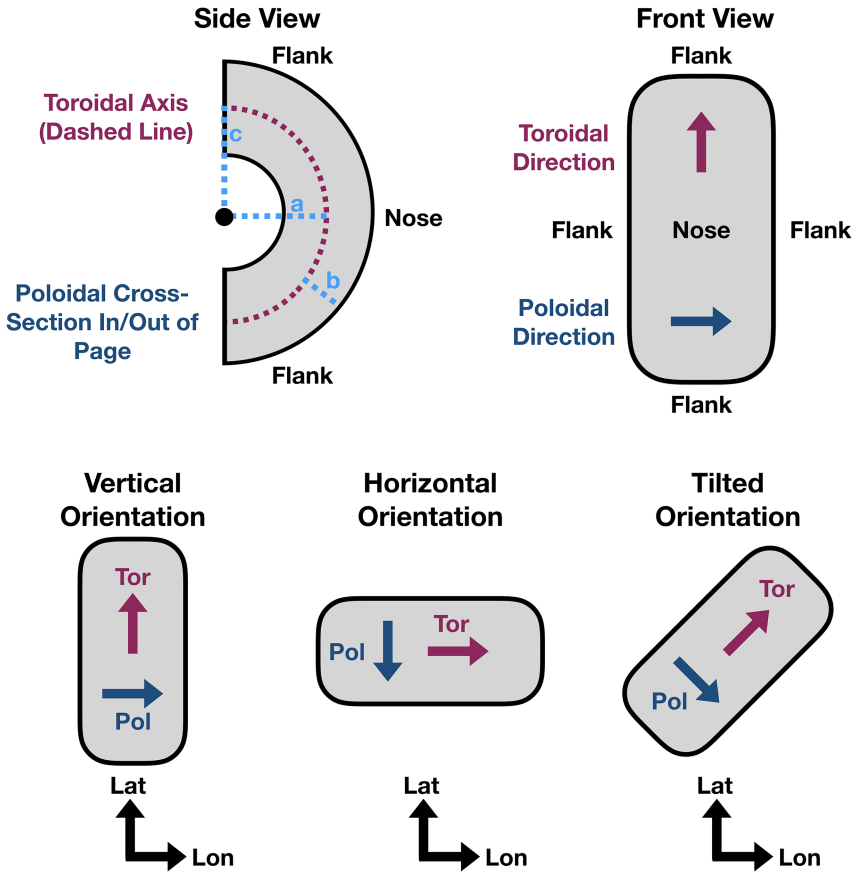

Figure 1. Cartoon showing a side view and a front view of the ANTEATR torus and illustrating the toroidal and poloidal directions (maroon and dark blue, respectively). The bottom illustrates how the toroidal and poloidal directions relate to the latitudinal and longitudinal directions for different CME orientations.

angular width AW= $\arctan((b+c)/(R-a-b)$, where R is the radial distance of the CME nose and two shape ratios $A = a/c$ and $B = b/c$.

We propagate the torus to 1 AU using the standard hydrodynamic drag equation.

$$F_d = C_d A \rho_{SW}(v_{CME} - v_{SW})|v_{CME} - v_{SW}|. \quad (1)$$

In equation (1), the drag force, F_d, is determined from the drag coefficient (C_d), the cross-sectional area of the CME in the direction of propagation (A), the background solar wind density (ρ_{SW}), the CME velocity (v_{CME}), and the solar wind velocity (v_{SW}). We will refer to the solar wind density by the number density n_{SW}, which we take to be the mass density divided by the proton mass. ANTEATR calculates a single force for the entire CME, which is assumed to propagate as a rigid torus. The net acceleration is determined by dividing the force by the CME mass, which uniformly decelerates the radial velocity of the entire CME (or accelerates in the case of CMEs slower than the background solar wind). This acceleration continually modifies the radial CME velocity as it propagates out, yielding a transit time and radial velocity upon impact. Note that throughout this work, we refer to the sensitivity of the arrival time and transit time interchangeably as the arrival time is simply the transit time added to the CME start time, and we do not consider variations in the start time.

In general, the determination of the transit time can be broken down into three factors. For the purposes of this illustration, we assume the CME is faster than the background solar wind. The first factor we will refer to as the "drag-free nose impact" transit time or T_0. This is the absolute minimum amount of time the CME could take to propagate to 1 AU, equivalent to the distance traveled divided by the coronal CME velocity. Still ignoring the effects of drag, the transit time will increase as the impact moves away from the nose toward

the flank, giving us the "drag-free actual impact" transit time or T_0'. Finally, the actual transit time, T, will further increase when drag is included and the CME velocity decreases during the transit.

For all models, T_0 will be the same if the same initial distance and velocity are used. Equation (1) is used by most drag-based models, including the simplification to a one-dimensional drag force. If T_0' is the same, A is calculated similarly, and the same background solar wind is used then these models should yield similar T. Models differ the most when it comes to how the CME shape is approximated, and therefore, the location of impact and the cross-sectional area differ as well, which will affect both T_0' and T.

ANTEATR differs from most drag-based models when it comes to determining the relative location of the CME and Earth or satellite of interest. We use the full three-dimensional shape and location to determine when impact first occurs rather than reducing the problem to one or two dimensions by taking a cut along the CME nose or along the expected direction of impact. Any uncertainty in this direction due to the inherent projection effect introduced by coronagraphs will affect the arrival time. In addition to exploring the sensitivity to parameters explicitly included in the drag equation, we will determine the extent to which the CME position influences the transit time. The simplifications in geometry introduced by other models could potentially cause errors in the arrival time on the scale of the variations induced by changes in the CME's three-dimensional position.

We wish to determine which parameters are the most critical for determining accurate arrival time predictions. This may vary from CME to CME, particularly for different size or speed CMEs. A CME that initially propagates at nearly the same speed as the background solar wind will not be affected the same as a CME initially much faster than the background solar wind. To account for this, we consider CMEs of different "strengths" and create an ensemble for each strength. We use the term strength to refer to a unique combination of CME mass, speed, and size, with weak CMEs being less massive, slower, and smaller than strong CMEs. We will refer to different strength CMEs by their kinetic energy, *KE*, or the base-10 logarithm of the KE in erg. While this parameter incorporates the changing velocity and mass at each strength, we emphasize that the angular width is simultaneously increasing.

We consider CMEs between masses of 10^{15} and 5×10^{16} g. Based on the properties of the observed CMEs used in Kay and Gopalswamy (2017), we determine linear scalings between the logarithm of the CME mass and the peak radial velocity and angular width

$$v = 660\log_{10}M_{\mathrm{CME}} - 9,475, \tag{2}$$

$$AW = 19.8\log_{10}M_{\mathrm{CME}} - 270, \tag{3}$$

where M_{CME} is in g and the resulting v and AW are in km/s and °, respectively. For our range of CME masses, this corresponds to velocities between 425 and 1,550 km/s and angular widths between 27 and 61°. These masses and velocities cause our CMEs having a log(KE) between 30.0 and 32.8, which ranges from roughly average to an extreme value (e.g., Gopalswamy et al., 2009).

Kay and Gopalswamy (2017) used the Graduated Cylindrical Shell stereographic reconstruction technique (Thernisien et al., 2006) to determine the angular width of the CMEs. This angular width is not the full angular width rather the angle between the nose and flank of the CME (half angle). As in Kay and Gopalswamy (2017), we use this angle to determine the span of our torus shape. In this work we use fixed values of 0.75 and 0.55 for the shape parameters A and B, the average of the cases in Kay and Gopalswamy (2017). When determining the sensitivity to the location of impact, we use b_{pol} and b_{tor}, which are the impact parameters in the poloidal and toroidal directions. We define these as between −100 and 100 with 0 representing the center in that cross-sectional direction and ±100 representing the edges. We find that our results are not particularly sensitive to the precise shape parameter values when we consider changes in terms of the impact parameters, though they certainly affect the conversion between impact parameter and degrees.

The ensembles are generated from a seed case by linearly sampling a range about each input parameter. The seed case for strength CME has a unique mass, velocity, and angular width, but all other parameters are the same. Table 1 lists the seed values with the superscript "a" indicating a value that scales with CME strength. For each strength ensemble, we vary each input parameter individually, running 30 simulations covering the range shown in Table 1. Each strength ensemble contains the seed case and eight sets of 20

Table 1
Seed Values and Ensemble Ranges

Parameter	Seed value	Range
b_{pol}	0	±100
b_{tor}	0	±100
v_{CME}[a]	425–1,550 km/s	±50%
M_{CME}[a]	10^{15}–5×10^{16} g	±50%
AW[a]	27–61°	±50%
v_{SW}	440 km/s	±25%
n_{SW}	6.9 cm^{-3}	±75%
C_d	1	±100%

[a]A value that scales with CME strength.

unique simulations, and we consider 30 different strengths. Note that for each strength case, the range for the velocity, mass, and AW are determined using ±50% of its specific seed values.

Typically when we run ANTEATR, we include the orbit of the Earth about the Sun, which causes roughly a degree change in longitude for each day of transit. Here we wish to focus on the change in transit time (Δt) rather than the absolute value, and this comparison is easiest when all impacts occur at the CME nose (except for the impact parameter study). To facilitate this, we exclude the orbital effects in this work. These secondary effects from small changes in the location of impact due to small changes in the Earth's orbital location are equivalent changes in the impact parameter of roughly a degree. The results of this work show that this magnitude of changes are negligible when the impact occurs near the CME nose.

3. Ensemble Results

We group our parameters into three sets: parameters related to the CME position, properties of the CME itself, and background solar wind properties. The results for these sets are shown in Figures 2–4 and discussed in sections 3.1–3.3. For each parameter, we first consider the percentage change in the transit time for a percentage change in the parameter. While percentages are not the most intuitive for forecasting, this normalization helps illuminate some of the trends across different strength CMEs. The ranges of the input parameters are not uniform between different parameters as we expect to be able to predict certain parameters more accurately than others. Table 1 shows these ranges. We also show the corresponding change in transit time for a given percentage change in input parameter. Finally, we use the information from each ensemble to derive the hourly change in transit time as a function of input parameter (in natural units) and CME strength.

Figures 2–4 all have the same format. Each row contains the results for an individual input parameter. Within that row, the left panel shows percentage change in transit time versus percentage change in input, the middle shows hourly change in transit time versus percentage change in input, and the right shows hourly change in transit time as a function of change in input parameter and CME strength (labeled according to the logKE).

In the left and middle panels, each point is colored according to the CME strength with darker colors representing average CMEs and brighter colors representing extreme CMEs. For each strength, we determine the transit time of the control case (unperturbed initial parameters) and subtract this from each ensemble member to determine the change in transit time. Positive changes indicate a delay in arrival time (longer transit time), and negative indicates early arrival. Dashed lines are shown every 10% (left panels) or 5 hr (middle panels) to illustrate the difference in scales between different parameters.

To facilitate comparison between different strength CMEs, we fit a natural cubic spline to each set. The resulting spline is shown by a line matching the color for that strength CME. Often polynomial and spline fits are subject to the Runge phenomena where the best fit oscillates wildly near the extreme points. Using a natural spline ensures that the fit is well behaved at near the edges by forcing a linear profile beyond the extreme points.

We use the spline fits to develop a continuous distribution of change in transit time as a function of change in input parameter and CME strength, which we show as a contour plot in the right panels. While the strength is labeled using the logKE, we remind that this represents a simultaneous change in mass, speed, and angular width. The contours are scaled to saturate at ±10 hr, the current average absolute uncertainty in arrival time predictions. Red indicates early arrivals, and blue indicates delays. Contour lines are drawn every 2 hr in change in arrival time, excluding 0 for readability. We allow for an extrapolation of 25% beyond the range used to fit the splines, a somewhat arbitrary but reasonable limit to the extent to which we can trust the interpolation. Gray-shaded regions indicate values outside this limit, which are likely beyond the range of uncertainty in the input parameters.

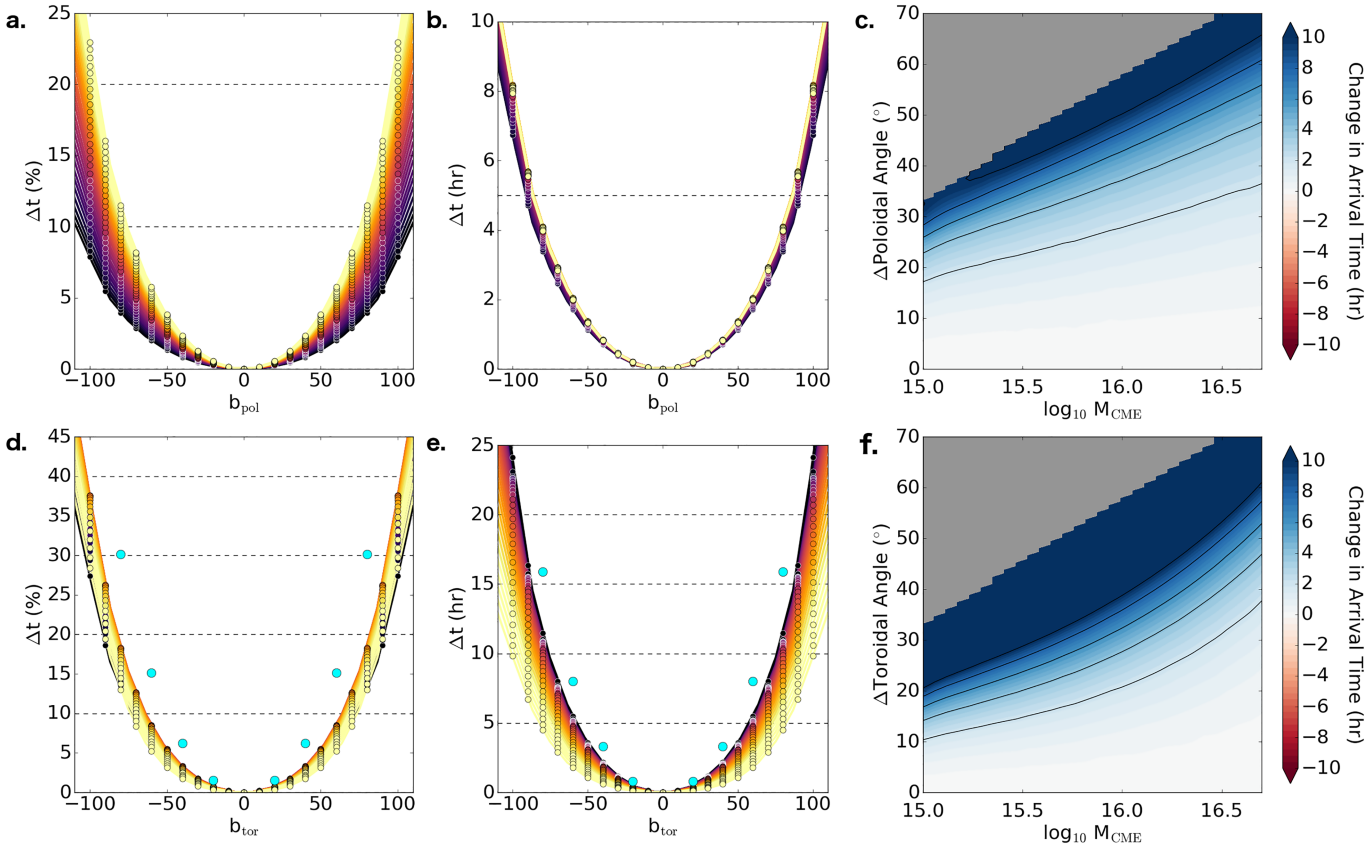

Figure 2. Sensitivity of transit time to positional input parameters. (a) and (d) show the percent change in transit time for a percent change in input parameter. (b) and (e) show the same in hours. In these panels the different colors indicate different strength CMEs with brighter colors representing more extreme CMEs. (c) and (f) show contours of change in transit time, in hours, for changes in inputs in natural units (e.g., degrees in this figure) and different size CMEs, labeled using the CME mass as a proxy. (a)–(c) show results for the poloidal impact parameter, and (d)–(f) show the toroidal impact parameter.

3.1. CME Position

For the position, we consider the impact parameter in either the toroidal or poloidal directions b_{pol} and b_{tor}. Our ensembles are centered about an impact directly at the CME nose, and our CME is horizontal so that the toroidal axis lies within the ecliptic plane. Accordingly, changes in latitude and longitude correspond respective to changes in the poloidal and toroidal directions. If we change the CME orientation, we see the same dependence on the toroidal and poloidal impact parameters, but these now correspond to different directions in terms of latitude and longitude. The bottom of Figure 1 illustrates how different CME orientations lead to the toroidal and poloidal directions corresponding to different combinations of the latitudinal and longitudinal directions.

Figure 2a shows that moving from the nose ($b_{pol} = 0$) to the extreme poloidal flank ($b_{pol} = \pm 100$) causes changes up to 25% in the transit time with the percentage increasing with CME strength. Since the transit time decreases with CME strength, we actually see little variation when the results are expressed in hours. The largest changes correspond to an 8 hr delay, as seen in Figure 2b. The transit time is particular insensitive to the position near the CME nose, any position out to about 60% of the poloidal width will produce a transit time within 2 hr of the control case. The sensitivity to precise position rapidly increases as the impact moves toward the flanks, changing by 4 hr for positions in the outer 40% of the poloidal radius.

The changes are much larger for the toroidal impact parameter, shown in the bottom row of Figure 2, since our CME shape extends much farther in the toroidal direction than the poloidal direction. We again find the results are more sensitive near the flanks than the nose. Looking at variations with CME strength, we find that the sensitivity initially increases as we move from the average cases toward the fast CMEs but then begins decreasing again as we continue toward the extreme CMEs. The powerful CMEs are physically larger and therefore have a greater difference between radial distance of the front at the nose and flank. Their

velocity is also faster, however, so it takes less time to cover a given distance. The turnover occurs when the speed outweighs the size and may occur at a different strength if using a different CME shape. The largest delays actually occur for the average CMEs, reaching about 25 hr despite only being a 27% change but having a long transit time.

Figures 2c and 2f show the contours of change in transit time extrapolated from the spline fits. Little change is observed for all strengths near the nose, only near the flanks does the transit time begin to change rapidly. For most masses, a change in position of 10° near the flanks can easily produce a 10 hr change in arrival time. Changes corresponding to the gray-shaded region in Figures 2c and 2f correspond to no impact occurring as one has moved beyond the extent of the CME. These factors make the CME position a very odd parameter when it comes to determining arrival time. For most cases, the results are insensitive, but for a small subset, the arrival time is extremely sensitive, and it can even lead to uncertainty in whether or not impact actually occurs.

Since our control cases impacts at the CME nose, changes in position, either poloidal or toroidal, can only result in a delay in transit time. Note that for predictions, if the impact was expected toward the flanks, then the uncertainty in position brings the impact closer to the flank or the nose, respectively, leading to either a delay or early arrival.

3.2. CME Parameters

In this section we consider changes in the CME speed, mass, and angular width. These are the same three parameters that change with our CME strength. Here, the control cases have the values corresponding to that strength, and then an individual parameter is varied, while the other two remain constant. All given values of log(KE) correspond to the seed values and do not reflect any changes from the parameter space explorations.

3.2.1. CME Velocity

In the top row of Figure 3, we look at the sensitivity to the CME velocity. Note that the behavior of equation (1) changes when the CME velocity drops below that of the background solar wind, causing an acceleration instead of a deceleration. All but our weakest control cases have CME velocities greater than the background solar wind speed, but when we consider decreases in the CME velocity, many ensemble members drop below it.

Changes to the CME velocity are the only changes we consider that affect the "drag-free nose impact" transit time T_0. An increase in velocity will decrease this time but will simultaneously also increase the drag force due to the larger difference from the background solar wind. The balance between these two effects determines the sensitivity to the CME velocity.

For all but the weakest few cases (below a log(KE) of 30.6), we see similar behavior for different strength CMEs with a slight increase in sensitivity toward higher strengths. If we look at changes in terms of hours, these effects again tend to balance out with CMEs with strengths above a log(KE) of 30.6 having a delay of 20 hr for a 50% decrease in CME velocity and an early arrival of 5 hr for a 50% increase in CME velocity.

The weakest cases show a rapid change in arrival time for small changes, but then the profiles flatten as the CME velocity approaches and ultimately falls below that of the background solar wind and the drag begins accelerating the CMEs.

Figure 3c shows contours for changes in the CME velocity. The spline plots suggest that and within the range shown in Figure 3c, the contours do saturate at ±10 hr for all strengths. The transit time is more sensitive to decreases in the CME velocity, which result in delayed arrival times. For the weakest CMEs, a change of less than 100 km/s causes a 10 hr change in the arrival time. This critical velocity increases with CME strength with a change of about 600 km/s (300 km/s) corresponding to an early (late) arrival of 10 hr for a log(KE) of 31.2 (10^{16} g) CME.

3.2.2. CME Mass

The middle row in Figure 3 shows results for changes in the CME mass. While this does not factor into the calculation of the drag force, it does determine the extent to which that force accelerates or decelerates the CME. As expected, as the mass increases, the drag force becomes less effective and the transit time decreases.

For the weakest CMEs, the velocities are essentially at the solar wind speed, so the drag force is small, and changes in the mass have a negligible effect. As the CME strength increases, so does the drag force and the

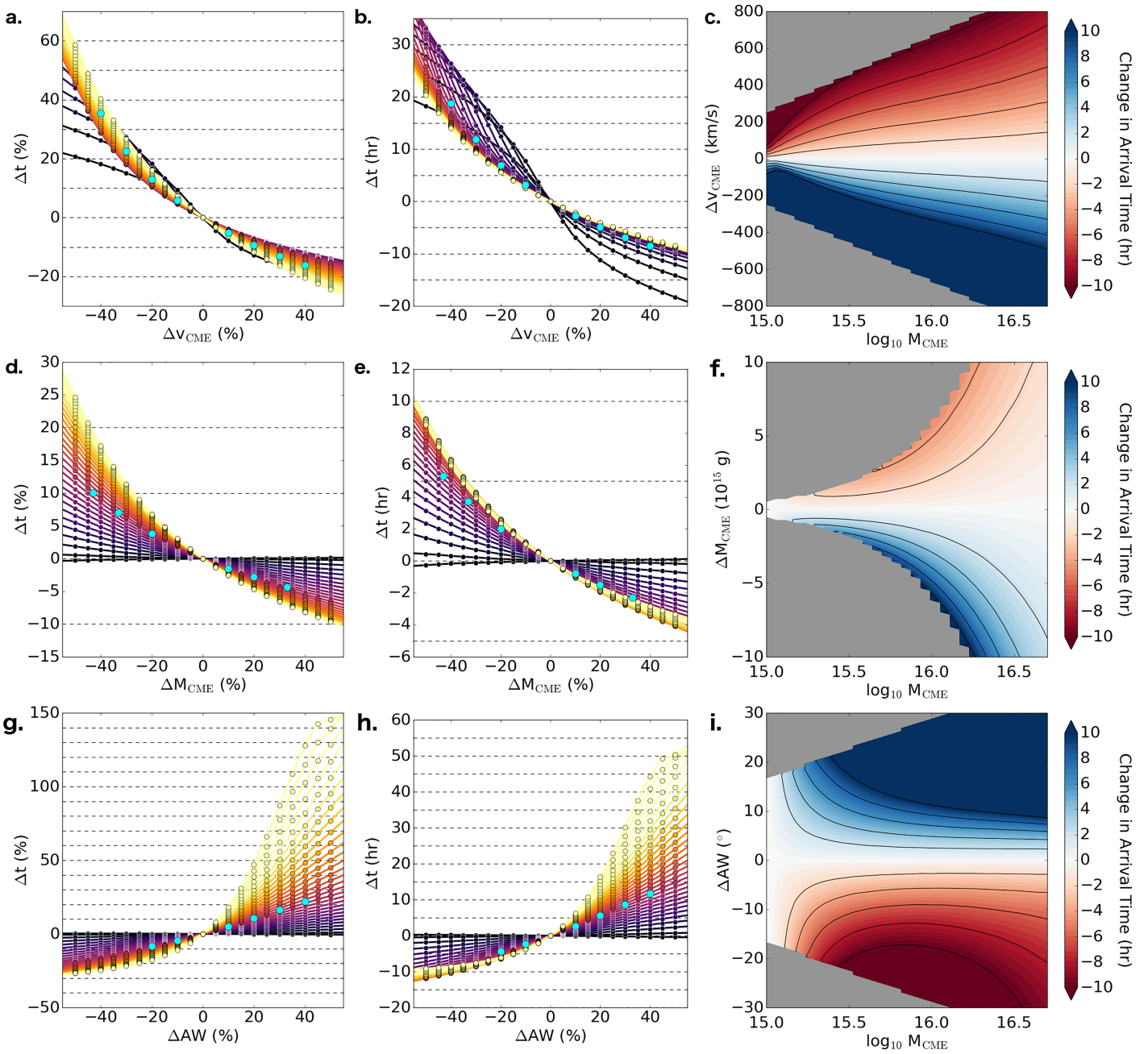

Figure 3. Same as Figure 2 but for the CME velocity (a–c), mass (d–f), and angular width (g–i).

transit time becomes more sensitive to changes the CME mass. For the most powerful CMEs, a decrease of 50% in the mass corresponds to a 25% delay, and increase of 50% corresponds to an early arrival by 10%. However, since these CMEs have the shortest transit times, these changes only correspond to a delay of 9 hr and an early arrival of 4 hr.

Figure 3f shows contours of the change in transit time for changes in mass up to 10^{16} g. Increases in mass cause early arrivals of less than 5 hr over the range of parameters considered. An increase in mass decreases the deceleration from the drag force, so the CMEs gradually approach the drag-free transit time. We find slightly stronger sensitivities to decreases in mass with values approaching a delay of 8 hr at the gray boundary. We note that while we choose not to extrapolate in this region, it already is very close to the fundamental limit of a 100% decrease in the CME mass. Accordingly, we suggest that in most cases, the CME mass is one of the least essential factors in determining accurate transit times.

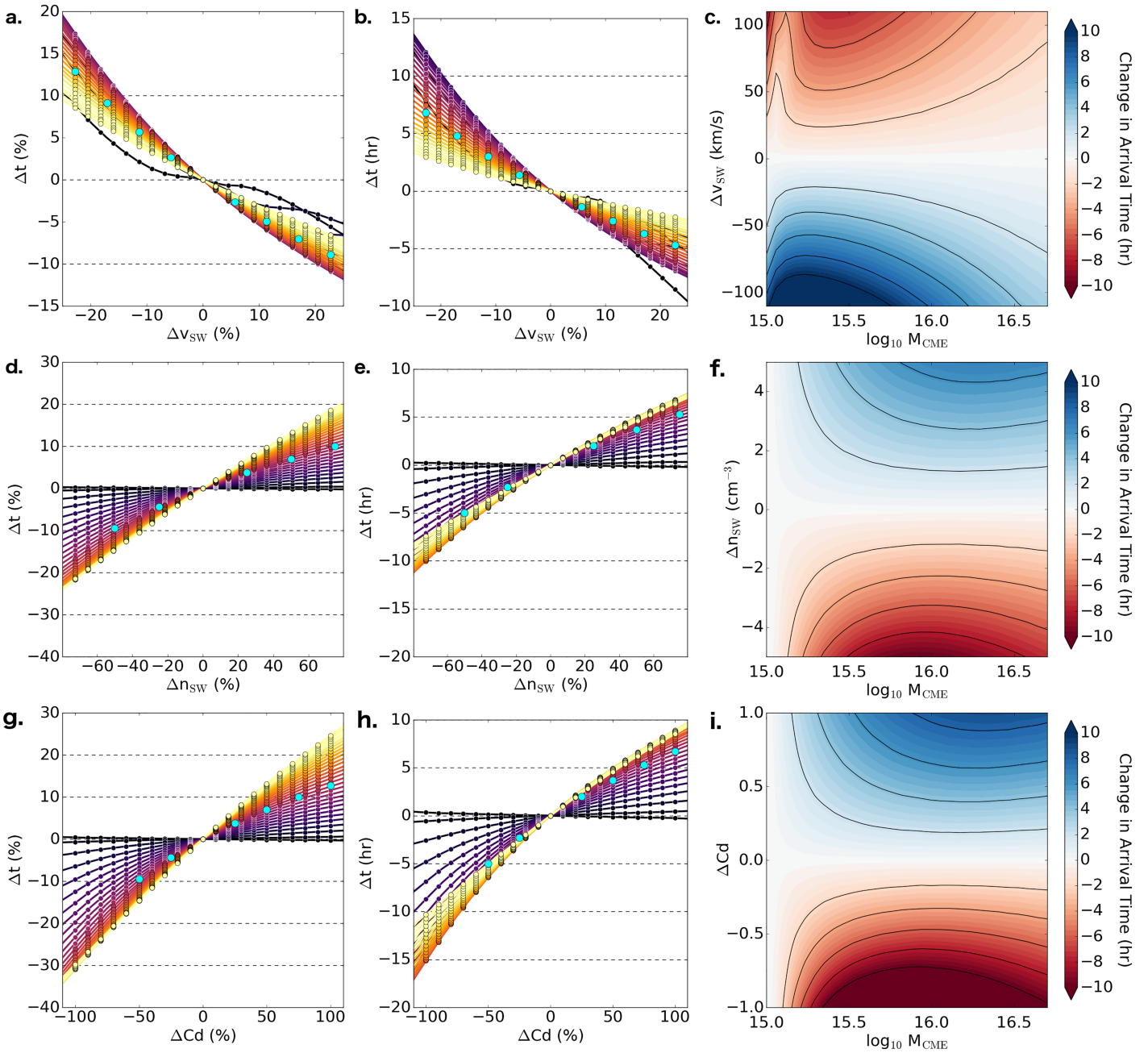

Figure 4. Same as Figure 2 but for the solar wind velocity (a–c), number density (d–f), and drag coefficient (g–i).

3.2.3. CME Angular Width

The final CME parameter we consider is the angular width, shown in the bottom row in Figure 3, which determines the cross-sectional area of the CME. Changes in the angular width cause the largest variation in transit time with early arrivals up to 30% of the total transit time for a decrease of 50% in the angular width and delays up to 150% for a 50% increase. The average CMEs again show little sensitivity due to the weak drag, but we see extreme delays for the most powerful CMEs. These CMEs have the largest differential speed from the background, and in the ANTEATR model, the area used in the drag force is roughly proportional to the square of the tangent of the angular width. The tangent rapidly increases as the angular width approaches 90°, and since the drag force depends on the square of it, it can very effectively decelerate the CME and cause a large delay of 50 hr if the angular width is underestimated by 30°.

In the contours in Figure 3i, we again see that the results are more sensitive to delays (larger angular width) than early arrivals (smaller angular width). Above a log (KE) of 31.1, an increase of 15° in the angular width causes a delay of 10 hr. In comparison, an early arrival of 10 hr typically requires a change in the angular width greater than 20°. For the weakest strengths, any change in the angular width causes a change of less than ±2 hr in the transit time.

3.3. Solar Wind Parameters

The previous parameters were all related to the CME itself, but the properties of the background solar wind may also play an important role in determining the transit time. For ANTEATR and similar to many other drag-based models, we use a simple solar wind that is fully determined by the velocity and number density at 1 AU. In this section we consider the effects of changes in the solar wind velocity, number density, and drag coefficient.

3.3.1. Solar Wind Velocity

The top row of Figure 4 shows that the sensitivity to the solar wind speed tends to increase as the CME strength decreases. For the average CMEs, where the CME velocity is comparable to the seed solar wind velocity, the trend breaks down as some of the ensemble members experience accelerations instead of decelerations. We found a similar breakdown for the weakest CMEs with the CME velocity in Figures 3a and 3b. For a CME with a log(KE) of 30.6, a decrease of 25% in the background solar wind speed causes a delay of 12 hr and an increase of 25% in the solar wind speed causes an early arrival of 7 hr.

Figure 4c shows that an accurate background solar wind speed is most critical for CME strength below a log(KE) of 30.9. For these smaller CMEs, a change of 100 km/s in the solar wind speed can cause an early arrival up to 8 hr or a delay up to 10 hr. The white strip in the top left corner of Figure 4c is where the solar wind speed is roughly equivalent to the CME speed and the sensitivity greatly decreases. The results are not particularly sensitive for large masses as a change of 100 km/s in the background speed represents a much smaller fractional change in the differential speed and therefore less change to the drag force.

3.3.2. Solar Wind Number Density

The middle row of Figure 4 shows the change in transit time for changes in the solar wind number density. We expect the solar wind density to be less certain than its velocity, so we consider a wider range of percent changes. For a given percentage change, the results tend to be less sensitive to the solar wind density than the solar wind speed. As for many parameters, the weakest CMEs show the least sensitivity because they undergo very little deceleration or acceleration since they begin propagation near the background solar wind speed.

The results are less sensitive to the density than for the solar wind velocity with a change of ±25% only causing changes of ±2–3 hr, but a decrease of 75% in the density causes a early arrival of 10 hr for moderate strength CMEs (around a log(KE) of 31.3). An increase of 75% causes an delay of 6–7 hr for similar strength CMEs .

The most sensitive region shifts toward higher masses for the background solar wind density, shown in Figure 4f. The majority of parameter space, however, corresponds to changes less than 6 hr. The largest changes are for a decreases of order 5 cm^{-3} at a log(KE) of 31.8, but our background solar wind model has a density of 6.9 cm^{-3} at 1 AU, so this corresponds to nearly depleting the entire density and a rather extreme uncertainty in background conditions.

A realistic solar wind background would likely have regions of different speeds and densities along the CMEs path, which is not currently incorporated into our model. This may suggest that the values found in this section should be considered lower limits on the uncertainty. If average values are chosen for the speed and density, however, the integrated effects from overestimates and underestimates may average out in terms of the net transit time. A better understanding of these intricacies would require study beyond the scope of this paper.

3.3.3. Drag Coefficient

The final parameter we consider is the drag coefficient. ANTEATR and other drag-based models use the standard form of drag used in hydrodynamics to describe the motion of a CME through a magnetized background, which was shown to be reasonable by the simulations of Cargill et al. (1996) and Cargill (2004). The drag coefficient is taken to be something near unity, similar to hydrodynamics, but this constant incorporates much of the subtleties of the actual physics involved and the precise value is poorly understood.

Kay and Gopalswamy (2018) found optimal arrival times using ANTEATR with a drag coefficient of 0.8 but only considered six CMEs.

Here we assume a control case with C_d =1 and explore values between 0 and 2. The bottom row of Figure 4 shows these results. As expected, the weakest CMEs are insensitive to C_d due to their minimal drag. For the strongest CMEs, we find that this causes a decrease of 30% in the transit time or an increase of 25%. The largest early arrivals of 15 hr occur for a CME mass near a log(KE) of 31.4, and the strongest CMEs have a delay of 9 hr.

Figure 4i shows the sensitivity to the background drag coefficient. The transit times are more sensitive to decreases in the drag coefficient. For CMEs with a log(KE) greater than about 30.5, the drag-free cases (ΔC_d of -1) have transit times differing from the control by more than 10 hr. An increase of one in the drag coefficient causes delays of 4–10 hr for similar strength CMEs. It is difficult to address the importance of uncertainty in the drag coefficient because we do not have a good measure of the actual range of that uncertainty. If we assume the traditional "near one" means between 0.5 and 1.5, then the uncertainty in the arrival time will be within ±4 hr. However, the sensitivity will greatly increase as the range of C_d expands.

4. Comparison With Other Models

We have suggested that these sensitivities should be representative for other drag-based models, and we test this using the DBM model (Vršnak & Žic, 2007), which is available for runs on demand in an online web application (http://oh.geof.unizg.hr/DBM/dbm.php). The online tool allows for some specification of CME and background parameters but differs slightly from ANTEATR in the input parameters. The DBM drag acceleration is calculated the same as in ANTEATR, but the drag coefficient C_d, CME area, solar wind density, and CME mass are combined into a single drag parameter Γ.

$$\Gamma = C_d \frac{A \rho_{SW}}{M_{CME}} \, 10^7 \text{ km}^{-1}. \tag{4}$$

The DBM default Γ of 2×10^{-8} km^{-1} is comparable to an ANTEATR CME of 5×10^{15} g (log(KE) of 31.3 and near the orange/purple transition in our color scheme and where the circle outlines switch from black to white in the spline plots). The comparison is not exact though as the CME shapes are prescribed differently with ANTEATR using a torus as compared to the DBM's cone shape with a rounded front. Where possible, we run DBM simulations using the equivalent changes in input parameters and show the results in Figures 2–4 with light blue circles. The DBM application restricts Γ to a minimum value of 0.1, which limits the range of our comparison in some cases. Note that while these figures show the similarity between the models in the change in transit time, the actual transit times for the control cases differ by about 6 hr between ANTEATR and DBM. We emphasize this comparison between models is only for the sensitivities to input parameters not the actual transit time values.

For the CME velocity (Figures 3a and 3b), mass (Figures 3d and 3e), angular width (Figures 3g and 3h), solar wind density (Figures 4a and 4b), and drag coefficient (Figures 4g and 4h), the DBM points fall directly on the equivalent ANTEATR results (orange/purple transition). Since the models use the same form of the drag equation, they scale similarly with input parameters.

For the CME position, we take the change in position along the toroidal axis to be more comparable to the changes for the DBM's axial symmetric shape. Figures 2d and 2e show the results for the change in position. We find that the results are similar, but the DBM tends to be slightly more sensitive, tending to exceed the ANTEATR sensitivity by about 5% or about 2 hr. This results from our toroidal direction having slightly flatter curvature than the DBM shape. We note that we get better agreement for the angular width than the position because we assume that the area and therefore Γ scales the same as the ANTEATR area.

We also find that ANTEATR is just slightly more sensitive to the background solar wind speed. For the DBM background model, the solar wind velocity and density are intrinsically coupled by assuming a constant mass flux. The solar wind velocity is the only parameter that can explicitly be modified, not the density or mass flux, so we account for changes in the density in Figures 4a and 4b by adjusting Γ. An increase in the DBM solar wind velocity causes a decrease in the density, which will decrease the transit time, nullifying some of the increase from the velocity increase. We emphasize that the difference in sensitivity between the

Table 2
Minimum Accuracy Needed for 5 Hr Arrival Time Accuracy

CME size	Poloidal position (°)	Toroidal position (°)	v_{CME} (km/s)	M_{CME} (10^{15} g)	AW (°)	v_{SW} (km/s)	n_{SW} (cm^{-3})	C_d	Γ (10^{-8} km^{-1})
Average	24.5	15.6	29	—	—	64	—	—	—
	8.0	3.5	−36	—	—	−80	—	—	
Fast	41.5	31.5	275	7.7	−7.3	110	−2.8	−0.40	−0.8
	13.5	7.5	−198	−3.8	6.0	−80	3.6	0.52	1.04
Extreme	53.0	50.0	400	—	−9.0	—	−3.4	−0.49	−0.98
	14.0	10.5	−283	—	5.0	—	3.8	0.55	1.10

two models is small, a decrease of 20% in the velocity corresponds to less than an hour difference between the delays of ANTEATR and DBM.

Finally, we comment on different combinations of variables used by other drag models, in particular, the sensitivity to Γ. Looking at equation (4), we find that we have essentially already explore the sensitivity to each of the individual components that factor into it. Changing either n_{SW} or C_d by a certain percentage is the same as changing Γ by that same percentage. Looking at Figures 4d and 4g, a change of −50% in either n_{SW} or C_d causes a 10% decrease in the transit time for the log(KE) of 31.3 and the DBM results. This corresponds to a change of 10^{-8} km^{-1} in Γ. The same information can be inferred from the mass or angular width, only with marginally more complicated math. Figure 4i can be most easily used to understand the expected sensitivity to Γ by simply multiplying the y axis values by 2×10^{-8} km^{-1}.

5. Discussion

We wish to use the information from the previous sections to develop suggestions on where the community should focus its efforts to improve arrival time predictions. We wish to find the accuracy with which parameters would need to be known for an accuracy of 5 hr. While this is a somewhat arbitrary value, it represents a factor of 2 improvement in the current mean absolute error. Table 2 shows these values for each parameter. For each size CME, the top row represents values that lead to an 5 hr early arrival, and the bottom row represents values that lead to a 5 hr delay. A dash indicates that no values within the range we consider can produce a 5 hr change that the transit time is not particularly sensitive to these parameters. We include values for Γ as well by scaling it from the results for C_d.

For an average CME (log(KE) 30.0, mass 10^{15} g, speed 425 km/s, and half-width 27°), we find the most critical parameter is the CME velocity, requiring an accuracy around 30 km/s or less. The solar wind velocity is also important, as can be the CME position if the impact is located near the flanks.

On the other hand, an extreme CME depends (log(KE) 32.8, mass 5×10^{16} g, speed 1,550 km/s, half-width 60°) most strongly on the angular width, requiring an accuracy of 5–10°. Our extreme case corresponds to a very large CME with a kinetic energy only a factor of 2.5 smaller than that estimated for the Carrington event (e.g., Cliver & Dietrich, 2013; Riley, 2012). We do not expect such an extreme event to occur as frequently as the average and fast cases. However, when an extreme CME does occur, an accurate measurement of the angular width is absolutely necessary. This will require coronagraph observations at a viewing angle off the Sun-Earth line, such as L4 or L5. We see that these extreme events will also be sensitive to the CME velocity, solar wind density, and drag coefficient. In the case of flank encounters, the position is again important.

We would expect to see CMEs comparable to the fast CME more frequently than the extreme case, particularly during high solar activity. Unfortunately, the accurate determination of the transit time of these CMEs seems to combine all the difficulties seen for the slower, average CMEs and more rare, extreme CMEs. Each of the parameters considered in this work can produce a 5 hr change in arrival time. Our instinct is that the angular width will likely be the limiting parameter for these CMEs as an accuracy below 7.5° should require stereoscopic measurements. These are the only CMEs for which the actual CME mass is a limiting factor, but we find that the required accuracy is roughly the same magnitude as the actual CME mass and reconstruction techniques tend to reproduce the mass within a factor of 2 (Vourlidas et al., 2010). Accurate estimations of the mass of Earth-directed CMEs again require a coronagraph with the Sun-Earth line near

the plane of the sky, though recent work shows promise in determining CME mass from EUV dimming (Dissauer et al., 2019; López et al., 2019; Mason et al., 2016).

For the position, we show the change in the location of impact along either the poloidal or toroidal direction that would be required to cause a 5 hr delay in the arrival time. For each mass CME, the top number is the critical value near the nose, and the bottom is the critical value near the flank. For all masses and both toroidal and poloidal directions, the results are much more sensitive near the flanks. The critical value near the nose tends to be 3–4 times larger than that near the flank. Both Mays et al. (2015) and Möstl et al. (2015) study the 7 January 2014 CME, a large CME that erupted near disk center and was expected to cause a large geomagnetic storm at Earth but ended up arriving 13 hr later and much weaker than expected. In hindsight, this CME was found to deflect away from disk center, moving the impact toward the flanks. This case study shows that, while not typically the largest source of error, the direction of propagation can certainly be important in individual events.

Pizzo et al. (2015) find similar behavior for ENLIL arrival time simulations. Weak-to-moderate CMEs tend to be the most sensitive to the CME velocity, whereas stronger CMEs are most sensitive to the angular width. Pizzo et al. (2015) also found that the sensitivity to CME parameters increased as the impact move away from the nose and toward the flanks, something we have not considered in this work. As such, we expect that the numbers in Table 2 could represent lower limits to the critical values needed for 5 hr accuracy.

Finally, we emphasize that the entirety of this work has considered the effects of varying a single parameter at a time. While this is useful for identifying the key parameters to focus on for immediate improvement in predictions, further study must be done to understand how uncertainty in multiple parameters compounds. In this work we have scratched the surface showing how the sensitivity changes for different "strength" CMEs, but this is only a first step as we assume uniform scaling of mass, speed, and size.

6. Conclusion

We have used the simple arrival time model ANTEATR to better understand how arrival time changes with various input parameters. We select a range representative of our current observational uncertainty in each input parameter and determine the corresponding range in arrival times. This information allows us identify to identify the most critical parameters for accurate arrival time predictions.

We produce results for CMEs of different "strengths," simultaneously varying the CME size, speed, and mass. For an average CME, we find the CME velocity is the most important parameter, whereas the angular width is most important for an extreme event. The transit time of a more common fast CME is affected by both the angular width and, to a lesser extent, the CME velocity. The CME position can have a strong influence on the transit time for all strength CMEs when impact occurs near the flanks. The position can also influence whether or not impact is expected to occur.

The background solar wind model is marginally important for all strength CMEs with the solar wind velocity tending to be more important for weaker CMEs and the solar wind density more important for faster CMEs. The effects from these solar wind parameters, however, tend not to be as large as those from the CME properties.

We compared the ANTEATR results with those from another drag-based model and find excellent agreement between the two. The actual transit time differs by a several hours between the two models, but the sensitivity to input parameters is nearly identical. The largest difference in sensitivity is for changes in CME position, which results from slight differences in the CME shape between models. This suggests that the sensitivities derived in this work can be reliably extended to other drag-based arrival time models.

Acknowledgments
C. K. is supported by the National Aeronautics and Space Administration under Grant 80NSSC19K0909 issued through the Heliophysics Early Career Investigators Program. C. V. is funded by the Research Foundation - Flanders, FWO SB PhD Fellowship 11ZZ216N. The ANTEATR model and the code used to generate the ensembles are available at github.com/ckay314/ANTEATR/releases/tag/v1.0 and are archived through Zenodo (https://doi.org/10.5281/zenodo.3533363).

References

Amerstorfer, T., Möstl, C., Hess, P., Temmer, M., Mays, M. L., Reiss, M. A., et al. (2018). Ensemble prediction of a halo coronal mass ejection using heliospheric imagers. *Space Weather*, *16*, 784–801. https://doi.org/10.1029/2017SW001786

Cargill, P. J. (2004). On the aerodynamic drag force acting on interplanetary coronal mass ejections. *Solar Physics*, *221*, 135–149. https://doi.org/10.1023/B:SOLA.0000033366.10725.a2

Cargill, P. J., Chen, J., Spicer, D. S., & Zalesak, S. T. (1996). Magnetohydrodynamic simulations of the motion of magnetic flux tubes through a magnetized plasma. *Journal of Geophysical Research*, *101*, 4855–4870. https://doi.org/10.1029/95JA03769

Cliver, E. W., & Dietrich, W. F. (2013). The 1859 space weather event revisited: Limits of extreme activity. *Journal of Space Weather and Space Climate*, *3*, A31. https://doi.org/10.1051/swsc/2013053

Dissauer, K., Veronig, A. M., Temmer, M., & Podladchikova, T. (2019). Statistics of coronal dimmings associated with coronal mass ejections. II. Relationship between coronal dimmings and their associated CMEs. *The Astrophysical Journal*, *874*(2), 123. https://doi.org/10.3847/1538-4357/ab0962

Dumbović, M., Čalogović, J., Vršnak, B., Temmer, M., Mays, M. L., Veronig, A., & Piantschitsch, I. (2018). The Drag-based Ensemble Model (DBEM) for coronal mass ejection propagation. *The Astrophysical Journal*, *854*, 180. https://doi.org/10.3847/1538-4357/aaaa66

Gopalswamy, N., Lara, A., Yashiro, S., Kaiser, M. L., & Howard, R. A. (2001). Predicting the 1-AU arrival times of coronal mass ejections. *Journal of Geophysical Research*, *106*, 29,207–29,218. https://doi.org/10.1029/2001JA000177

Gopalswamy, N., Yashiro, S., Michalek, G., Stenborg, G., Vourlidas, A., Freeland, S., & Howard, R. (2009). The SOHO/LASCO CME Catalog. *Earth Moon and Planets*, *104*, 295–313. https://doi.org/10.1007/s11038-008-9282-7

Hess, P., & Zhang, J. (2015). Predicting CME ejecta and sheath front arrival at L1 with a data-constrained physical model. *The Astrophysical Journal*, *812*, 144. https://doi.org/10.1088/0004-637X/812/2/144

Jin, M., Manchester, W. B., van der Holst, B., Sokolov, I., Tóth, G., Vourlidas, A., et al. (2017). Chromosphere to 1 AU simulation of the 2011 March 7th event: A comprehensive study of coronal mass ejection propagation. *The Astrophysical Journal*, *834*, 172. https://doi.org/10.3847/1538-4357/834/2/172

Kay, C., & Gopalswamy, N. (2017). Using the coronal evolution to successfully forward model CMEs' in situ magnetic profiles. *Journal of Geophysical Research: Space Physics*, *122*, 11,810–11,834. https://doi.org/10.1002/2017JA024541

Kay, C., & Gopalswamy, N. (2018). The effects of uncertainty in initial CME input parameters on deflection, rotation, B_z, and arrival time predictions. *Journal of Geophysical Research: Space Physics*, *123*, 7220–7240. https://doi.org/10.1029/2018JA025780

Kay, C., Opher, M., & Evans, R. M. (2015). Global trends of CME deflections based on CME and solar parameters. *The Astrophysical Journal*, *805*, 168. https://doi.org/10.1088/0004-637X/805/2/168

Liu, J., Ye, Y., Shen, C., Wang, Y., & Erdélyi, R. (2018). A new tool for CME arrival time prediction using machine learning algorithms: CAT-PUMA. *The Astrophysical Journal*, *855*, 109. https://doi.org/10.3847/1538-4357/aaae69

López, F. M., Cremades, H., Balmaceda, L. A., Nuevo, F. A., & Vásquez, A. M. (2019). Estimating the mass of CMEs from the analysis of EUV dimmings. *Astronomy & Astrophysics*, *627*(A8), 9. https://doi.org/10.1051/0004-6361/201834163

Mason, J. P., Woods, T. N., Webb, D. F., Thompson, B. J., Colaninno, R. C., & Vourlidas, A. (2016). Relationship of EUV irradiance coronal dimming slope and depth to coronal mass ejection speed and mass. *The Astrophysical Journal*, *830*(1), 20. https://doi.org/10.3847/0004-637X/830/1/20

Mays, M. L., Thompson, B. J., Jian, L. K., Colaninno, R. C., Odstrcil, D., Möstl, C., et al. (2015). Propagation of the 7 January 2014 CME and resulting geomagnetic non-event. *The Astrophysical Journal*, *812*, 145. https://doi.org/10.1088/0004-637X/812/2/145

Möstl, C., Rollett, T., Frahm, R. A., Liu, Y. D., Long, D. M., Colaninno, R. C., et al. (2015). Strong coronal channelling and interplanetary evolution of a solar storm up to Earth and Mars. *Nature Communications*, *6*, 7135. https://doi.org/10.1038/ncomms8135

Napoletano, G., Forte, R., Moro, D. D., Pietropaolo, E., Giovannelli, L., & Berrilli, F. (2018). A probabilistic approach to the drag-based model. *Journal of Space Weather and Space Climate*, *8*, A11. https://doi.org/10.1051/swsc/2018003

Odstrcil, D., Pizzo, V. J., Linker, J. A., Riley, P., Lionello, R., & Mikic, Z. (2004). Initial coupling of coronal and heliospheric numerical magnetohydrodynamic codes. *Journal of Atmospheric and Solar-Terrestrial Physics*, *66*(15-16), 1311–1320. https://doi.org/10.1016/j.jastp.2004.04.007

Paouris, E., & Mavromichalaki, H. (2017). Effective acceleration model for the arrival time of interplanetary shocks driven by coronal mass ejections. *Solar Physics*, *292*, 180. https://doi.org/10.1007/s11207-017-1212-2

Pizzo, V. J., de Koning, C., Cash, M., Millward, G., Biesecker, D. A., Puga, L., et al. (2015). Theoretical basis for operational ensemble forecasting of coronal mass ejections. *Space Weather*, *13*, 676–697. https://doi.org/10.1002/2015SW001221

Pomoell, J., & Poedts, S. (2018). EUHFORIA: European heliospheric forecasting information asset. *Journal of Space Weather and Space Climate*, *8*, A35. https://doi.org/10.1051/swsc/2018020

Riley, P. (2012). On the probability of occurrence of extreme space weather events. *Space Weather*, *10*, S02012. https://doi.org/10.1029/2011SW000734

Riley, P., Mays, M. L., Andries, J., Amerstorfer, T., Biesecker, D., Delouille, V., et al. (2018). Forecasting the arrival time of coronal mass ejections: Analysis of the CCMC CME scoreboard. *Space Weather*, *16*, 1245–1260. https://doi.org/10.1029/2018SW001962

Rollett, T., Möstl, C., Isavnin, A., Davies, J. A., Kubicka, M., Amerstorfer, U. V., & Harrison, R. A. (2016). ElEvoHI: A novel CME prediction tool for heliospheric imaging combining an elliptical front with drag-based model fitting. *The Astrophysical Journal*, *824*(2), 131. https://doi.org/10.3847/0004-637X/824/2/131

Shiota, D., & Kataoka, R. (2016). Magnetohydrodynamic simulation of interplanetary propagation of multiple coronal mass ejections with internal magnetic flux rope (SUSANOO-CME). *Space Weather*, *14*, 56–75. https://doi.org/10.1002/2015SW001308

Thernisien, A. F. R., Howard, R. A., & Vourlidas, A. (2006). Modeling of flux rope coronal mass ejections. *The Astrophysical Journal*, *652*, 763–773. https://doi.org/10.1086/508254

Verbeke, C., Mays, M. L., Temmer, M., Bingham, S., Steenburgh, R., Dumbović, M., et al. (2019). Benchmarking CME arrival time and impact: Progress on metadata, metrics, and events. *Space Weather*, *17*, 6–26. https://doi.org/10.1029/2018SW002046

Vourlidas, A., Howard, R. A., Esfandiari, E., Patsourakos, S., Yashiro, S., & Michalek, G. (2010). Comprehensive analysis of coronal mass ejection mass and energy properties over a full solar cycle. *The Astrophysical Journal*, *722*, 1522–1538. https://doi.org/10.1088/0004-637X/722/2/1522

Vršnak, B., & Žic, T. (2007). Transit times of interplanetary coronal mass ejections and the solar wind speed. *Astronomy and Astrophysics*, *472*, 937–943. https://doi.org/10.1051/0004-6361:20077499

Vršnak, B., Žic, T., Vrbanec, D., Temmer, M., Rollett, T., Möstl, C., et al. (2013). Propagation of interplanetary coronal mass ejections: The drag-based model. *Solar Physics*, *285*, 295–315. https://doi.org/10.1007/s11207-012-0035-4

Wold, A. M., Mays, M. L., Taktakishvili, A., Jian, L. K., Odstrcil, D., & MacNeice, P. (2018). Verification of real-time WSA-ENLIL+Cone simulations of CME arrival-time at the CCMC from 2010 to 2016. *Journal of Space Weather and Space Climate*, *8*(27), A17. https://doi.org/10.1051/swsc/2018005

Xie, H., Ofman, L., & Lawrence, G. (2004). Cone model for halo CMEs: Application to space weather forecasting. *Journal of Geophysical Research*, *109*, A03109. https://doi.org/10.1029/2003JA010226